Stability Analysis of fMRI BOLD Signals for Disease Diagnosis

Honorine Niyigena Ingabire, Haibo Qu, Min Li, Sixuan He, Joan Toluwani Amos, Yan Cui, Qing Wang, Dezhong Yao, Dan Ma, and Peng Ren

***Abstract*— Previous studies have demonstrated that the stability changes in physiological signals can reflect individuals' pathological conditions. Apart from this, according to system science theory, a large-scale system can generally be divided into many subsystems whose stability level govern its overall performance. Therefore, this study attempts to investigate the possibility of analyzing the stability of decomposed subsystems of resting-state fMRI (rs-fMRI) BOLD signals in order to assess the overall characteristic of the human brain and individuals' health conditions. We used attention deficit/hyperactive disorder (ADHD) as an example to illustrate our method. Rs-fMRI BOLD signals were first decomposed into dynamic modes (DMs) which can illuminate the patterns of brain subsystems. Each DM is associated with one eigenvalue that determines its stability as well as oscillation frequency. Accordingly, we divided the DMs within common BOLD frequency bands into stable and unstable DMs. Then, the features related to the stability of those DMs were extracted, and nine common classifiers were used to differentiate healthy controls from ADHD patients taken from ADHD-200, a well-known dataset. The results showed that almost all features were statistically significant. Additionally, our proposed approach outperforms all existing methods with the highest possible precision, recall, and area under the receiver operating characteristic curve of 100%. In sum, we are the first to evaluate the stability of BOLD signals and demonstrate its possibility for disease diagnosis. This method can unveil new mechanisms of brain function, and could be widely used in medicine and engineering.**

***Index Terms*— Attention-deficit/hyperactive disorder (ADHD), blood oxygen level dependent (BOLD), dynamic mode decomposition (DMD), functional magnetic resonance imaging (fMRI), stability, subsystems.**

I. Introduction

FUNCTIONAL magnetic resonance imaging (fMRI) is a non-invasive and ionization-free technique which essentially utilizes blood oxygen level dependent (BOLD) contrast to reflect brain activity by capturing the changes in cerebral blood flow and oxygenation concentration (known as hemodynamic response) related to the energy required by neurons due to a certain task (such as memory or cognition) or during resting state [1]. Activation of a particular brain region induces an increase in the blood flow to that region, then deoxyhemoglobin in nearby blood vessels are replaced by oxyhemoglobin. The diamagnetic property of oxyhemoglobin leads to the generation of high-intensity of magnetic resonance signal due to its reduced interference with the magnetic field compared to that of deoxyhemoglobin (which is paramagnetic). Thus, the BOLD contrast mechanism occurs as a result of the differentiated magnetic properties of deoxygenated and oxygenated blood. Therefore, this mechanism is used to reveal the neurons which are activated at any given time.

fMRI was primarily used as a task-based scan to capture the changes in cerebral blood flow and oxygenation concentration (associated with specific task) which can be reflected in BOLD contrast. Later, Biswal *et al.* found that spontaneous BOLD signal generated by neurons while subjects are at rest reflects their baseline BOLD variance [2]. Resting-state fMRI (rs-fMRI) is a relatively novel method which is based on detecting spontaneous low-frequency oscillations of the BOLD signal, usually less than 0.1 Hz, over time. Task-state and rs-fMRI have been widely used in neuroscience and clinical research. However, rs-fMRI is easy to implement, demands little cooperation, reveals multiple brain networks, and does not require any explicit task. Thus, studies have shown that rs-fMRI has many advantages compared to task-based fMRI, particularly in

Manuscript received April 14, 2021; revised November 14, 2021; accepted March 25, 2022. Date of publication April 1, 2022; date of current version April 19, 2022. This work was supported in part by the National Natural Science Foundation of China under Grant 62171109 and Grant 82121003, in part by the Sichuan Science and Technology Program under Grant 2020YFS0094, and in part by the University of Electronic Science and Technology of China. *(Honorine Niyigena Ingabire and Haibo Qu contributed equally to this work.) (Corresponding authors: Dezhong Yao; Dan Ma; Peng Ren.)*

Honorine Niyigena Ingabire, Min Li, Sixuan He, Joan Toluwani Amos, and Peng Ren are with the Sichuan Provincial People's Hospital, MOE Key Laboratory for Neuroinformation, School of Life Science and Technology, University of Electronic Science and Technology of China, Chengdu 611731, China (e-mail: pren28@uestc.edu.cn).

Haibo Qu is with the Department of Radiology, West China Second University Hospital, Sichuan University, Chengdu 610017, China.

Yan Cui is with the Department of Neurosurgery, Sichuan Provincial People's Hospital, University of Electronic Science and Technology of China, Chengdu 610072, China, and also with the Sichuan Translational Medicine Research Hospital, Chinese Academy of Sciences, Chengdu 610072, China.

Qing Wang is with Neuro Data Science-ORIGAMI Laboratory, McConnell Brain Imaging Centre, McGill University, Montreal, QC H3A 2B4, Canada.

Dezhong Yao is with the Sichuan Provincial People's Hospital, MOE Key Laboratory for Neuroinformation, School of Life Science and Technology, University of Electronic Science and Technology of China, Chengdu 611731, China, and also with the Research Unit of Neuroinformation, Chinese Academy of Medical Sciences, Chengdu 611731, China (e-mail: dyao@uestc.edu.cn).

Dan Ma is with the Department of Rehabilitation Medicine, West China Second University Hospital, Sichuan University, Chengdu 610041, China (e-mail: yoyoma38@163.com).

Digital Object Identifier 10.1109/TNSRE.2022.3164074

studies involving patients with brain abnormalities including strokes, tumors, traumatic injuries, paralysis, and attention deficit [3]–[5]. Therefore, this study only considers rs-fMRI signals.

A. Stability Analysis of Physiological Signals

Stability is an inherent property of a system, reflecting its ability to maintain or recover its original structure, or to function under internal or external disturbance. Stability analysis is not only essential in system science (or cybernetics), but has also been applied in fields including industrial manufacturing, product design, and power systems [6]–[9]. Furthermore, it has recently been widely applied in the field of neuroscience. Micro-level studies have showed that changes in synaptic firing patterns are closely related to the brain disorders. For instance, loss of synapses in brains of Alzheimer's disease patients leads to decreases in firing rate, which consequently change the stability of neural networks by altering their dynamic patterns [10]. Furthermore, Hocepied *et al.* found that epileptic patients have more unstable electroencephalography signals than those of healthy subjects [11].

Furthermore, previous studies have shown that the stability of other physiological signals, such as respiratory signal and blood oxygen saturation, can be used to determine an individual's health condition. For example, abnormal breathing patterns were successfully extracted from a patient with sleep apnea by simply evaluating the stability of that individual's heart rate, breathing patterns, and blood oxygen saturation [12]. Therefore, Glass *et al.* even proposed that the majority of pathological conditions occur as a result of unstable physiological signals [13].

Although the stability of various physiological signals has been analyzed, no studies have yet evaluated the stability of fMRI BOLD signals. This study attempts to examine this, for the following reasons: (1) Changes in neuronal firing rate have been found to strongly parallel changes in cerebral blood flow, which can be reflected in BOLD signals [1]. As mentioned previously, instability in neuronal firing patterns mostly occurs due to the presence of pathologies. (2) Measured fMRI BOLD signals are widely used in neuroscience and clinical studies because of their potential to capture dynamic characteristics of the brain. Thus, we hypothesize that analyzing the stability of BOLD signals could reveal new brain mechanisms and potentially reflect individuals' health conditions.

B. Dynamic Mode Decomposition

Dynamic Mode Decomposition (DMD) is a data-driven approach that extracts the most relevant spatial information together with corresponding temporal information, from complex large-scale data by regarding linear combinations of spatial patterns at previous time points as the spatial pattern of the observed data at the subsequent point [14]. This method was first used to analyze fluid flows in fluid mechanics [15], and has recently drawn attention in many other fields, such as disease modeling and robotics [16]. Additionally, it has been successfully employed to analyze brain-related signals. For instance, Brunton *et al.* successfully extracted sleep spindle networks by applying DMD algorithm on large-scale sleep electrocorticography data [17]. Similarly, epileptic seizures were accurately detected using the electroencephalography signals of epileptic patients, by measuring the power of the dynamic modes (DMs) of these signals at different frequency bands [18]. Furthermore, Casorso *et al.* initially implemented this method to analyze resting-state and motor-task fMRI data, and successfully identified the classical resting-state, task-state, and new task-state networks together with their additional temporal characteristics [19]. Kunert-Graf *et al.* also applied DMD together with unsupervised clustering on rs-fMRI data, and successfully characterized spatial-temporal patterns of individual's resting-state networks [20].

Although these previous studies successfully implemented DMD for fMRI analysis, they only focused on its spatiotemporal patterns. The stability of DMs of BOLD signals have not yet been evaluated. Therefore, this study attempts to analyze BOLD signals based on their stable and unstable DMs decomposed by DMD. This was inspired by the following reasons: (1) The human brain is considered as a complex large-scale system, and its dynamic behaviors can be captured by recorded rs-fMRI BOLD signals in macroscopic quantities. Therefore, medical studies have successfully applied decomposition methods such as independent component analysis (ICA) and principal component analysis (PCA) to extract the most significant information from fMRI data [5], [21], [22]. In contrast with those traditional fMRI signal decomposition methods, only DMD is able to extract components and their stabilities from dynamic and high-dimensional data. (2) Apart from this, according to system science theory, complex large-scale systems can generally be divided into many subsystems, whose stability determines the overall performance [23]. In the case of human brain, the DMs decomposed from rs-fMRI BOLD signals by DMD can reflect the underlying patterns of brain subsystems. Thus, it is necessary to evaluate how the macro-dynamic patterns of fMRI BOLD signals are affected by the stability of their subsystems, which has not yet been investigated by previous studies. Therefore, this study attempts to analyze fMRI data based on stable and unstable DMs of BOLD signals, which may not only help to illuminate new brain mechanisms, but may also contribute to research on mental disorders.

C. Attention-Deficit/Hyperactive Disorder

Due to the number of brain disorders, it would be impossible for this study to implement our proposed approach on all of them. Therefore, patients with attention-deficit/hyperactive disorder (ADHD) are taken as an example to illustrate the effectiveness of our approach. One of the most common neurobehavioral disorders, ADHD normally first occurs during childhood and lasts into adulthood. It is estimated that approximately 5-10% of preschool and school-aged children suffer from this disorder [24]. ADHD patients lack attention and control, which leads to problems such as social integration, unnecessary risk-taking, and memory impairment, which can consequently lead to financial hardship for families and an

enormous burden on society. Similar to many other brain disorders, the underlying mechanism of ADHD is still not fully understood. Different methods have been proposed to highlight the brain mechanisms of ADHD patients using rs-fMRI, including ICA, PCA, graph theory, correlation, clustering, and neural networks [25]–[35]. For example, Tabas *et al.* identified the differences between ADHD patients and healthy subjects by combining independent components and a spatial variant of the Fisher's linear discriminant [26]. References [28]–[30] classified ADHD based on different graph-based measures. Also, ADHD has been classified by measuring the brain's functional connectivity using different correlation-based methods, including Pearson's correlation, and partial correlation [31]–[33]. Other studies applied different deep neural network on whole-brain connectivity for ADHD classification [27], [35].

Although much effort has been made to study ADHD, its automatic detection is still challenging. Currently, its diagnosis is based on clinical-subjective symptoms, including inattention, hyperactivity, and impulsivity. Therefore, this study proposes a novel approach for rs-fMRI data analysis, which is based on stability analysis of subsystems of BOLD time series. We hypothesize that our proposed approach may not only reveal new mechanisms underlying the functional connectivity of the brain, but also can effectively improve the diagnosis of brain disorders.

This study's flow chart is shown in Fig. 1. First, the preprocessed rs-fMRI BOLD time series were segmented into short overlapping windows. The DMD algorithm was then used to decompose individual window data into stable and unstable DMs. Then, features corresponding to the stability level of these DMs were extracted, and the differences between the stability degree of DMs of ADHD patients and HCs were investigated by implementing statistical tests on each extracted feature. Finally, the classification performance of our proposed approach was evaluated using nine well-known classifiers.

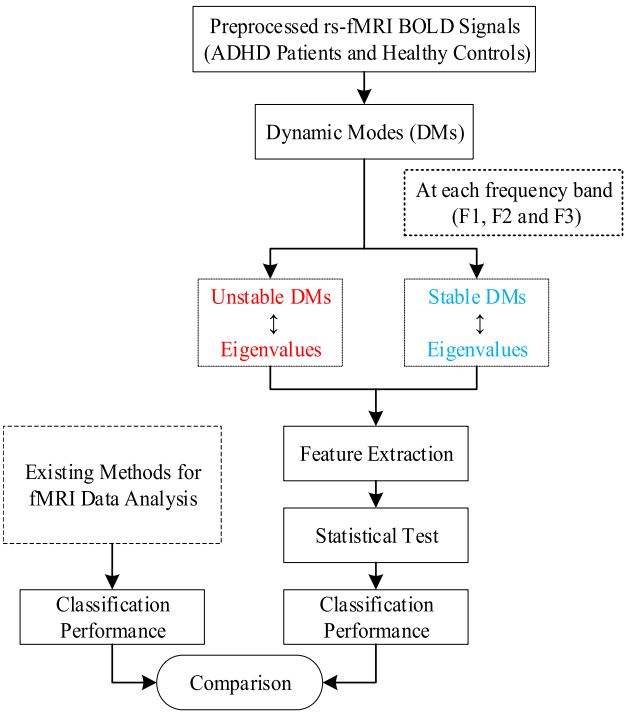

Fig. 1. The flow chart of this study. We analyze DMs within three different frequency bands: F1 (0.009-0.027 Hz), F2 (0.027-0.073 Hz), and F3 (0.009-0.08 Hz). Note: classification performance includes specificity, sensitivity, accuracy, and area under the receiver operating characteristic curve (AUC).

II. Materials and Methods

A. Data Description

The rs-fMRI data used to evaluate our proposed approach were taken from a common database, namely the Neuro Bureau ADHD-200 database [36]. This database contains data from eight imaging sites: Bradley Hospital/-Brown University, Kennedy Krieger Institute (KKI), NeuroImage (NI), New York University Child Study Center (NYU), Oregon Health Sciences University (OHSU), Peking University (Peking), University of Pittsburgh, and Washington University at Saint Louis. Because Bradley Hospital/ Brown University, Washington University at Saint Louis, and University of Pittsburgh do not provide fMRI data from ADHD patients, this study used the data from five imaging sites (KKI, NYU, NI, Peking, and OHSU) for further analysis. These imaging sites not only comprise different number of subjects, but also acquired rs-fMRI data using different parameters and equipment, which makes the dataset quite diverse and provides an opportunity to develop new robust models for ADHD diagnosis. A global competition was held for classification of ADHD subjects, and preprocessed data, including training and test sets of each imaging site, were provided by the consortium.

We used the preprocessed time series data of 954 region of interests (ROIs) (resulting from ROI 1000 parcellation) preprocessed using NeuroImaging Analysis Kit pipeline [36]. During preprocessing, the first three volumes were removed to allow magnetization to reach equilibrium, site-specific slice timing correction to the middle slice was performed, and the parameters of a rigid-body motion between each time frame and the median volume of a run were estimated, followed by spatial resampling across frames. Next, the fMRI time series were corrected from slow time drifts (using high-pass filter) and physiological noise (using an automated labeling of noise components in individual independent component analysis). Then, for each subject, median volume of one selected fMRI run was co-registered with corresponding structural-MRI scan using Minctracc. The brain was also parcellated into 954 ROIs, covering the grey matter using region-growing algorithm based on the iterative merging of mutual-nearest neighbors. Finally, average time series for each ROI were extracted. Based on previous studies which used this dataset for fMRI analysis, we also considered the BOLD components within the frequency range of 0.009-0.08 Hz for further analysis [22], [28], [34]. In addition, following previous studies, subjects whose scans exhibited artifacts based on the performance of quality control provided in the phenotypic information, were excluded for further analysis [28], [34]. The demographic information and the number of subjects for each group by imaging site are shown in Table I.

TABLE I
DEMOGRAPHIC INFORMATION FOR THE ADHD-200 DATA SAMPLES USED IN THIS STUDY

Site	Total subjects	Diagnostic status	Sex (M / F)	Age Mean / stdev
Training dataset				
NYU	177	HC	87 (43 / 44)	12.5 / 3.1
		ADHD	90 (69 / 21)	11.5 / 2.7
KKI	78	HC	58 (31 / 27)	10.3 / 1.3
		ADHD	20 (11 / 9)	10.3 / 1.6
NI	39	HC	22 (10 / 12)	17.5 / 2.4
		ADHD	17 (15 / 2)	17.0 / 2.8
Peking	183	HC	109 (65 / 44)	11.9 / 1.4
		ADHD	74 (70 / 4)	12.3 / 1.7
OHSU	183	HC	47 (17 / 25)	8.9 / 1.1
		ADHD	37 (26 / 11)	8.7 / 1.0
Test dataset				
NYU	41	HC	12 (8 / 4)	11.7 / 2.9
		ADHD	29 (20 / 9)	10.2 / 2.5
KKI	11	HC	8 (7 / 1)	10.5 / 1.1
		ADHD	3 (3 / 0)	8.7 / 0.6
NI	25	HC	14 (1 / 13)	20.3 / 3.2
		ADHD	11 (11 / 0)	16.9 / 2.1
Peking	51	HC	27 (13 / 14)	10.2 / 1.8
		ADHD	24 (19 / 5)	11.3 / 1.9
OHSU	34	HC	28 (13 / 15)	10.3 / 1.3
		ADHD	6 (5 /1)	10.3 / 1.6

Note: M and F denote male and female, respectively; stdev represents standard of deviation.

B. Computation of the Dynamic Mode Decomposition

DMD is an equation-free governing decomposition method used to investigate the dynamic systems of large-scale data. This approach has the advantage of extracting a set of DMs that possesses both spatial and temporal patterns from a multivariate time series. The DMD algorithm was refined by Tu *et al.*., and is summarized below [37].

Consider measurements recorded from n locations at times $k\Delta t$, where a column vector $\mathbf{x}_k$ contains the measurements at snapshot k. For example, in the case of rs-fMRI data, these measurements may denote BOLD time series data from n ROIs sampled every Δt (repetition time). The measurements from m snapshots in time (sampling points) can be arranged into two $n \times (m-1)$ raw data matrices $\mathbf{X}$ and $\mathbf{X}^s$ raw data matrices as follows:

$$\mathbf{X} = \begin{pmatrix} x_{11} & \cdots & x_{1(m-1)} \\ \vdots & \ddots & \vdots \\ x_{n1} & \cdots & x_{n(m-1)} \end{pmatrix} = [\,\mathbf{x}_1 \quad \cdots \quad \mathbf{x}_{m-1}\,] \tag{1}$$

$$\mathbf{X}^s = \begin{pmatrix} x_{12} & \cdots & x_{1m} \\ \vdots & \ddots & \vdots \\ x_{n2} & \cdots & x_{nm} \end{pmatrix} = [\,\mathbf{x}_2 \quad \cdots \quad \mathbf{x}_m\,] \tag{2}$$

According to the textbook *'Dynamic mode decomposition: data-driven modeling of complex systems,'* $\mathbf{X}^s$ is calculated by shifting the columns of $\mathbf{X}$ by a single Δt as shown above [38]. Therefore, an overlap exists between the observed data of these matrices.

DMD assumes the existence of a linear operator $\mathbf{H}$, which determines the temporal progression from $\mathbf{X}$ to $\mathbf{X}^s$ such that:

$$\mathbf{X}^s = \mathbf{H}\mathbf{X} \tag{3}$$

The eigendecomposition of this operator $\mathbf{H}$ generates the dynamic mode decomposition of these consecutive matrices, $\mathbf{X}$ and $\mathbf{X}^s$. The data matrix $\mathbf{X}$ is assumed to have high-dimensional snapshots, i.e., the measurements n at each snapshot are far greater than the number of snapshots m, thus transition matrix $\mathbf{H}$ (with the size $n \times n$) can be regarded as a high-dimensional linear regression of the nonlinear dynamics that governs the relationship between $\mathbf{X}$ and $\mathbf{X}^s$. As a consequence, computing the eigendecomposition of $\mathbf{H}$ is not straightforward. Fortunately, the DMD algorithm utilizes a low dimensional matrix $\tilde{\mathbf{H}}$ resulting from the projection of $\mathbf{H}$ onto the leading singular vectors of $\mathbf{X}$ to carry out decomposition of $\mathbf{H}$ based on the following steps:

Step 1: Calculate the singular value decomposition (SVD) of the raw data matrix:

$$\mathbf{X} \approx \mathbf{U}\mathbf{\Sigma}\mathbf{V}^* \tag{4}$$

where $\mathbf{U}$, $\mathbf{\Sigma}$, and $\mathbf{V}$ respectively denote left singular vectors, singular values, and right singular vectors. Then, substitute (4) into (3) to obtain the SVD of $\mathbf{X}^s$:

$$\mathbf{X}^s = \mathbf{H}\mathbf{U}\mathbf{\Sigma}\mathbf{V}^* \tag{5}$$

Step 2: Approximate matrix $\mathbf{H}$ by computing the pseudoinverse of $\mathbf{X}$ using its SVD:

$$\mathbf{H} \approx \mathbf{X}^s\mathbf{X}^{-1} \triangleq \mathbf{X}^s\mathbf{V}\mathbf{\Sigma}^{-1}\mathbf{U}^* \tag{6}$$

Step 3: Compute a low dimensional matrix $\tilde{\mathbf{H}}$ by projecting $\mathbf{H}$ onto the proper orthogonal modes of $\mathbf{U}$:

$$\tilde{\mathbf{H}} = \mathbf{U}^*\mathbf{H}\mathbf{U} = \mathbf{U}^*\mathbf{X}^s\mathbf{V}\mathbf{\Sigma}^{-1} \tag{7}$$

Step 4: Calculate the eigendecomposition of $\tilde{\mathbf{H}}$ as follows:

$$\tilde{\mathbf{H}}\mathbf{W} = \mathbf{W}\mathbf{\Lambda} \tag{8}$$

where the columns of the matrix $\mathbf{W}$ denote the eigenvectors of $\tilde{\mathbf{H}}$, and $\mathbf{\Lambda}$ is a diagonal matrix whose elements are the eigenvalues of the full matrix $\mathbf{H}$ as well as the data matrix $\mathbf{X}$.

Step 5: Compute the DMs of $\mathbf{X}$ using the time-shifted matrix $\mathbf{X}^s$ and eigenvectors $\mathbf{W}$:

$$\mathbf{\Phi} = \mathbf{X}^s\mathbf{V}\mathbf{\Sigma}^{-1}\mathbf{W} \tag{9}$$

Notably, the columns of $\mathbf{\Phi}$ represent the DMs or eigenvectors of the high-dimensional operator $\mathbf{H}$, and each DM $\boldsymbol{\phi}_j$ corresponds to an eigenvalue λ_j $(j = 1, \ldots, K)$ in diagonal matrix $\mathbf{\Lambda}$ as shown in [37], where K denotes the total number of DMs.

Finally, an approximation of the observed data can be regarded as a simple dynamic model $\widehat{\mathbf{X}}(t)$:

$$\mathbf{X}(t) \approx \widehat{\mathbf{X}}(t) = \mathbf{\Phi}\exp(\mathbf{\Omega}t)\mathbf{g} \tag{10}$$

where a diagonal matrix $\mathbf{\Omega} = \log(\mathbf{\Lambda})/\Delta t$ contains the eigenvalues in continuous time, t denotes the time, and the vector $\mathbf{g}$ has the weights matching the first measured time point such that $\mathbf{g} = \mathbf{\Phi}^{-1}\mathbf{x}_1$.

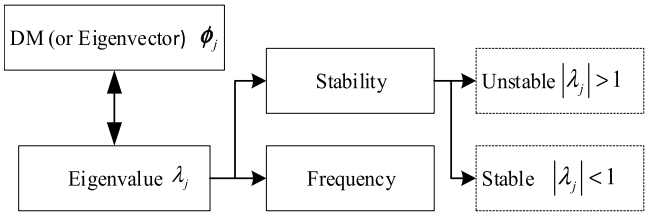

Fig. 2. The steps for computing the stability of DMs and their corresponding frequencies.

Note that both $\mathbf{\Phi}$ and $\mathbf{\Lambda}$ are complex values, and $\widehat{\mathbf{X}}$ generally possesses non-zero imaginary components. Thus, the eigenvalues can be written as $\lambda_j = r_j^{i\omega_j}$, where ω_j and r_j (elements of $\mathbf{\Omega}$) represent the damping frequency and ratio of $\boldsymbol{\phi}_j$, respectively. Each DM oscillates at frequency f_j, and can be computed using the imaginary part of ω_j as shown below:

$$f_j = \left| \frac{imag(\omega_j)}{2\pi} \right| \tag{11}$$

According to the theory of discrete time linear systems, the magnitude of the eigenvalue determines whether the system is stable or unstable. When $|\lambda_j| < 1$, the system is regarded as asymptotically stable, otherwise it is unstable [39]. Therefore, each eigenvalue determines the stability and frequency of its corresponding DM (see Fig. 2).

In this study, we divided all the decomposed DMs into stable or unstable DMs within three common frequency bands of rs-fMRI BOLD signal, i.e. F1 (0.009-0.027 Hz), F2 (0.027-0.073 Hz), and F3 (0.009-0.08Hz) (See Fig. 3 for an example). These bands were only chosen for the following reasons: (1) As mentioned above, this study used fMRI time series taken from ADHD-200. The database provides preprocessed fMRI time series within 0.009-0.08 Hz (F3). In addition, previous studies used this database for analysis of fMRI data considering BOLD components within frequency band F3. In order to easily compare our proposed method with the state-of-the art methods, we also follow the same strategy for further analysis [22], [28], [34]. (2) It has been suggested that the sub-components of the BOLD signal at frequency bands 0.009-0.027 Hz (F1) and 0.027-0.073 Hz (F2) can provide different information for understanding the mechanisms underlying brain function [40]–[43]. For example, in [42], BOLD components within F2 provided essential information to distinguish ADHD patients from healthy subjects. Furthermore, the oscillatory signals associated with resting-state functional connectivity were found to be mainly located within F1 and F2 Hz [43]. Therefore, we analyzed BOLD components within frequency bands F1, F2 and F3 separately for further analysis.

In the case of fMRI BOLD time series from n ROIs ($n = 954$ in this study), their decomposed stable and unstable DMs together with their corresponding eigenvalues are demonstrated as follow:

$$\mathbf{\Phi} = \left[\mathbf{\Phi}^{unst}, \mathbf{\Phi}^{st}\right] \Leftrightarrow \mathbf{\Lambda} = \begin{bmatrix} \mathbf{\Lambda}^{unst} & 0 \\ 0 & \mathbf{\Lambda}^{st} \end{bmatrix} \tag{12}$$

where $\mathbf{\Phi}^{unst}$ is the matrix whose columns are unstable DMs, and their corresponding eigenvalues are in the diagonal matrix

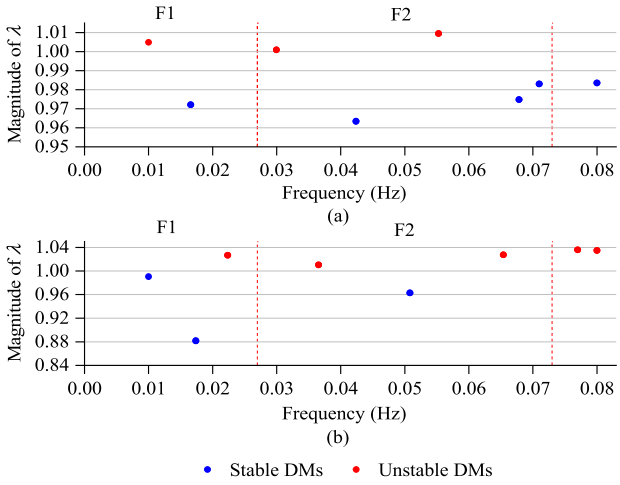

Fig. 3. An example of the oscillatory frequencies and magnitudes of eigenvalues of DMs for BOLD signals. (a) one HC; and (b) one ADHD patient. The Horizontal axis shows the DMs of BOLD signals oscillating at different frequencies (F1: 0.009-0.027 Hz, F2: 0.027-0.073 Hz, and F3: 0.009-0.08 Hz) computed using their corresponding eigenvalues (see (11)). The vertical axis illustrates the eigenvalues' magnitudes corresponding to the DMs of the BOLD signals, which determine whether the DM is stable when its corresponding eigenvalue $|\lambda_j| < 1$ (shown in blue), or it is unstable if $|\lambda_j| > 1$ (shown in red). It is worth noting that distribution of oscillatory frequencies and magnitudes of the eigenvalues of the DMs of the BOLD signals of the above subjects conforms to the trends of the other subjects.

$\mathbf{\Lambda}^{unst}$ as shown below:

$$\mathbf{\Phi}^{unst} = \left[\boldsymbol{\phi}_1^{unst}, \ldots, \boldsymbol{\phi}_d^{unst}, \ldots, \boldsymbol{\phi}_D^{unst}\right] \tag{13}$$

$$\mathbf{\Lambda}^{unst} = \begin{bmatrix} \lambda_1^{unst} & 0 & \cdots & \cdots & 0 \\ 0 & \ddots & \ddots & \ddots & \vdots \\ \vdots & \ddots & \lambda_d^{unst} & \ddots & \vdots \\ \vdots & \ddots & \ddots & \ddots & 0 \\ 0 & \cdots & \cdots & 0 & \lambda_D^{unst} \end{bmatrix} \tag{14}$$

where $\boldsymbol{\phi}_d^{unst}$ is a vector representing the unstable DM, and its corresponding eigenvalue is denoted by element λ_d^{unst}. $d = 1, 2, \ldots, D$, and D indicates the total number of unstable DMs. Each element of $\boldsymbol{\phi}_d^{unst}$, namely $\boldsymbol{\phi}_d^{unst}(p)$, corresponds to each ROI, where $p = 1, 2, \ldots, 954$. At the same time, the columns of $\mathbf{\Phi}^{st}$ represent stable DMs, and their corresponding eigenvalues are shown in the diagonal matrix $\mathbf{\Lambda}^{st}$ as follows:

$$\mathbf{\Phi}^{st} = \left[\boldsymbol{\phi}_1^{st}, \ldots, \boldsymbol{\phi}_c^{st}, \ldots, \boldsymbol{\phi}_C^{st}\right] \tag{15}$$

$$\mathbf{\Lambda}^{st} = \begin{bmatrix} \lambda_1^{st} & 0 & \cdots & \cdots & 0 \\ 0 & \ddots & \ddots & \ddots & \vdots \\ \vdots & \ddots & \lambda_c^{st} & \ddots & \vdots \\ \vdots & \ddots & \ddots & \ddots & 0 \\ 0 & \cdots & \cdots & 0 & \lambda_C^{st} \end{bmatrix} \tag{16}$$

where a vector $\boldsymbol{\phi}_c^{st}$ denotes the stable DM, and the element λ_c^{st} represents its corresponding eigenvalue, $c = 1, 2, \ldots, C$, and C is the total number of stable DMs. Each element of $\boldsymbol{\phi}_c^{st}$, namely $\boldsymbol{\phi}_c^{st}(p)$, is associated with an individual ROI. It is worth noting that according to the textbook '*Dynamic mode*

decomposition: data-driven modeling of complex systems', the first singular values which account for over 85% of the total variance of the data should be selected [38]; this study follows the same strategy and the number of eigenvalues of all subjects (which is equal to the number of DMs) was approximately 15. Also, for each subject, number of stable DMs C and unstable DMs D of the BOLD signals vary with time. Therefore, the values of C and D are not fixed.

C. Feature Extraction

We first implemented DMD on short sliding windows of BOLD signals. Specifically, DMs were computed within 32-frame windows sliding by 4 frames in each time interval. This window size was chosen in accordance with a recent study which also applied DMD on rs-fMRI data [20]. For each window, we divided DMs at each frequency band (F1, F2, and F3) into a set of stable and unstable DMs, as described above. Then, three types of features were extracted: (1) the ratio of unstable DMs to the whole set of DMs, (2) the features extracted from eigenvalues, (3) the features extracted from DMs (or eigenvectors). The first feature was extracted to evaluate the ratio of unstable DMs to the total DMs as shown below:

$$R_D = \frac{D}{D+C} \tag{17}$$

Then, the parameters were derived from the eigenvalues, because they can generally capture information inherent to their corresponding DMs. We extracted these parameters as follows. The parameter reflecting the relationship between the eigenvalues of unstable and stable DMs:

$$R_{\mathbf{\Lambda}} = \frac{\sum_{d=1}^{D} \left|\lambda_d^{unst}\right|}{\sum_{d=1}^{D} \left|\lambda_d^{unst}\right| + \sum_{c=1}^{C} \left|\lambda_c^{st}\right|} \tag{18}$$

where $R_{\mathbf{\Lambda}}$ indicates the ratio of magnitudes of eigenvalues of their corresponding unstable DMs to the whole set of DMs. Similarly, we evaluated the fast convergent and divergent DM by respectively computing the eigenvalue magnitudes of the most and least stable DMs $\lambda_{\min}$ and $\lambda_{\max}$ as follows:

$$\lambda_{\min} = \min\left(\left|\Lambda^{st}\right|\right) \tag{19}$$

$$\lambda_{\max} = \max\left(\left|\Lambda^{unst}\right|\right) \tag{20}$$

Finally, we extracted the features from DMs. The DMs generally illuminate the relationships among ROIs. Each element of 954 $\times$ 1 DM $\boldsymbol{\phi}_d^{unst}$ or $\boldsymbol{\phi}_c^{st}$, namely $\boldsymbol{\phi}_d^{unst}(p)$ or $\boldsymbol{\phi}_c^{st}(p)$, contains two essential pieces of information: the magnitude of the element, which measures the participation of the ROI within the DM (subsystem), and the phase, which reflects the oscillatory phase of an individual ROI relative to others at that DM's frequency. In other words, the magnitude and phase of each DM can indicate the activity level of the ROIs within that dynamic pattern. Therefore, this study attempted to employ the magnitudes and the phases of stable and unstable DMs as important information for BOLD signals. We examined the ratio of magnitudes and phases of the unstable DMs within the total DMs as shown below:

$$R_{\boldsymbol{\phi}}^{M} = \frac{\sum_{p=1}^{954}\sum_{d=1}^{D} \left|\boldsymbol{\phi}_d^{unst}(p)\right|}{\sum_{p=1}^{954}\sum_{d=1}^{D} \left|\boldsymbol{\phi}_d^{unst}(p)\right| + \sum_{p=1}^{954}\sum_{c=1}^{C} \left|\boldsymbol{\phi}_c^{st}(p)\right|} \tag{21}$$

$$R_{\boldsymbol{\phi}}^{P} = \frac{\sum_{p=1}^{954}\sum_{d=1}^{D} angle\left(\boldsymbol{\phi}_d^{unst}(p)\right)}{\sum_{p=1}^{954}\sum_{d=1}^{D} angle\left(\boldsymbol{\phi}_d^{unst}(p)\right) + \sum_{p=1}^{954}\sum_{c=1}^{C} angle\left(\boldsymbol{\phi}_c^{st}(p)\right)} \tag{22}$$

where $R_{\boldsymbol{\phi}}^{M}$ and $R_{\boldsymbol{\phi}}^{P}$ indicate the overall ratios of the magnitudes and oscillatory phases of the 954 ROIs of the unstable DMs to those of all DMs, respectively. Furthermore, for each ROI, we calculated average of its magnitude and phase in stable DMs as follows:

$$\boldsymbol{M}_{roi}^{st} = \frac{\sum_{c=1}^{C} \left|\boldsymbol{\phi}_c^{st}\right|}{C} \tag{23}$$

$$\boldsymbol{P}_{roi}^{st} = \frac{\sum_{c=1}^{C} angle\left(\boldsymbol{\phi}_c^{st}\right)}{C} \tag{24}$$

where $\boldsymbol{M}_{roi}^{st}$ and $\boldsymbol{P}_{roi}^{st}$ are both vectors (with size 954 $\times$ 1) whose elements $\boldsymbol{M}_{roi}^{st}(p)$ and $\boldsymbol{P}_{roi}^{st}(p)$ respectively denote the averaged magnitude and phase of the individual ROIs in the stable DMs. Finally, we computed the average magnitude and phase of each ROI in the unstable DMs $\boldsymbol{M}_{roi}^{unst}(p)$ and $\boldsymbol{P}_{roi}^{unst}(p)$, as shown below:

$$\boldsymbol{M}_{roi}^{unst} = \frac{\sum_{d=1}^{D} \left|\boldsymbol{\phi}_d^{unst}\right|}{D} \tag{25}$$

$$\boldsymbol{P}_{roi}^{unst} = \frac{\sum_{d=1}^{D} angle\left(\boldsymbol{\phi}_d^{unst}\right)}{D} \tag{26}$$

Notably, the decomposition of BOLD signals provides complex conjugate pairs of DMs as well as of eigenvalues, hence, the phases of each pair of modes are also conjugate. Consequently, the observed results in (24) and (26) will be zero. In order to address this problem, for each DM, we subtracted the phase of the first ROI from those of the other ROIs, then we computed the average of the relative phases of all DMs. It is also worth noting that for statistical and classification analysis, we calculated the average of these newly developed parameters from all windows of each subject's BOLD signals.

D. Statistical Analysis

For each BOLD frequency band, we applied the Jarque-Bera test on each feature extracted above to evaluate normality at the 0.05 significance level, and found that only a few of the extracted features follow a normal distribution. Therefore, we implemented a Wilcoxon rank-sum test to evaluate the

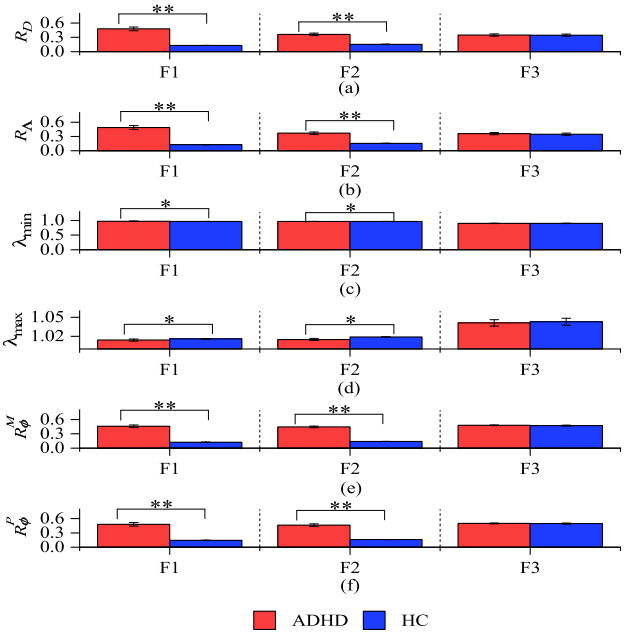

Fig. 4. The means and standard deviations of our six derived features for each BOLD frequency band of ADHD patients and HCs. (a) R_D represents the ratio of the number of stable DMs to the total DMs (see (17)); (b) R_Λ denotes the ratio of eigenvalue's magnitude of unstable DMs to those of the total DMs (see (18)); (c) λ_{min} represents an eigenvalue of the most stable DM (see (19)); (d) λ_{max} represents an eigenvalue of the most unstable DM (see (20)); (e) R_ϕ^M denotes the overall ratio of the magnitudes of all 954 ROIs of unstable DMs to the total DMs (see (21)); (f) R_ϕ^P represents the overall ratio of the oscillatory phases of 954 ROIs of unstable DMs to the total DMs (see (22)) (After the Bonferroni correction, $^*p < 0.05$, $^{**}p < 10^{-10}$).

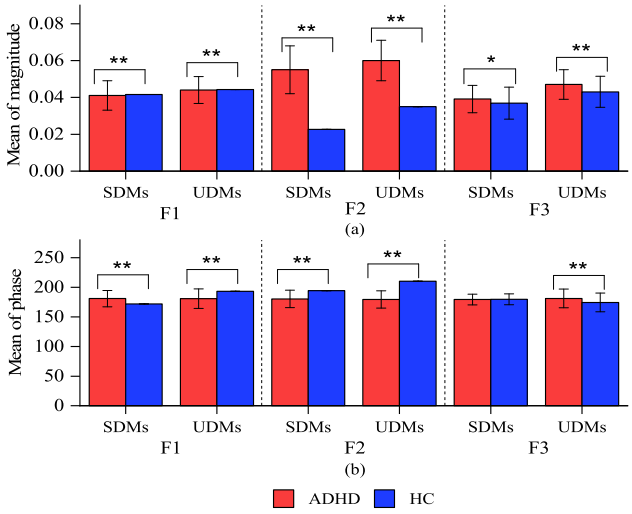

Fig. 5. The averages of the four derived features (i.e. magnitudes and phases of all 954 ROIs in stable and unstable DMs $\boldsymbol{M}_{roi}^{st}$, $\boldsymbol{M}_{roi}^{unst}$, $\boldsymbol{P}_{roi}^{st}$, and $\boldsymbol{P}_{roi}^{unst}$ see (23)-(26)) of BOLD signals of ADHD patients and HCs at each frequency band. (After the Bonferroni correction: $^*p < 0.05$, $^{**}p < 10^{-10}$). Note: SDMs: Stable DMs; UDMs: Unstable DMs.

difference of those extracted parameters between ADHD patients and HCs. After applying Bonferroni correction, the features with p value < 0.05 were then considered significant.

E. Classification

As illustrated in Fig. 5, we used the average magnitudes and phases associated with all ROIs in stable and unstable DMs of BOLD signals of ADHD patients and HCs at each frequency band in order to evaluate the stability changes of the whole brain. Thus, for the classification, a total of ten features which shown in Fig. 4 and Fig. 5, were used to assess the performance of our proposed approach. This performance was evaluated using nine well-known classifiers: k-nearest neighbor (KNN), Naïve Bayes, multilayer perceptron (MLP), support vector machine (SVM), logistic, stochastic gradient descent (SGD), random forest (RF), AdaBoost, and Bayes Net [44]–[49].

We used the open-source software Waikato Environment for Knowledge Analysis (WEKA) to build the aforementioned classifiers [50]. The default hyperparameters values of each classifier in WEKA have been widely used for classification and have demonstrated good generalization ability. This study also used the default mode of WEKA for classification (refer to supporting material for more details). The proposed approach was evaluated using training and test sets provided by the ADHD-200 database. For the training set, 10-fold stratified cross-validation (CV) was used to assess the model's performance. First, each dataset of the aforementioned sites was divided into ten equally-sized subsets. Then, one of the subsets was tested using a model trained on the remaining nine. This procedure was repeated until every subset was used once for testing. Then, the overall accuracy, precision, recall and area under the curve (AUC) for the classifier was calculated using the average performance over the ten classification runs. For the test set, the hold-out approach was used to evaluate the classification performance. First, the model was trained using training set, then tested using the test set. Finally, the performance parameters specificity, sensitivity, accuracy, and AUC were used to evaluate the effectiveness of our proposed approach for fMRI data analysis.

III. Results

In this study, DMD is implemented on rs-fMRI BOLD time series of both ADHD patients and HCs from each imaging site independently. Since, the scanning parameters and equipment of those sites were different, therefore their subjects cannot be combined for analysis, as mentioned previously. Notably, the statistical results of the data from all imaging sites exhibited similar trend. Thus, we only showed the statistical results of the data from NYU.

A. Statistical Analysis

For each BOLD frequency band (F1, F2, and F3), we found that most of the extracted features were significant, especially in the frequency bands F1 and F2. In general, as illustrated in Fig. 4, the DMs of BOLD signals of ADHD patients at frequency bands F1 and F2 were found to be less stable compared to those of HCs.

Also, as shown in Table II, comparing the HC group with ADHD patients, the number of ROIs with significant

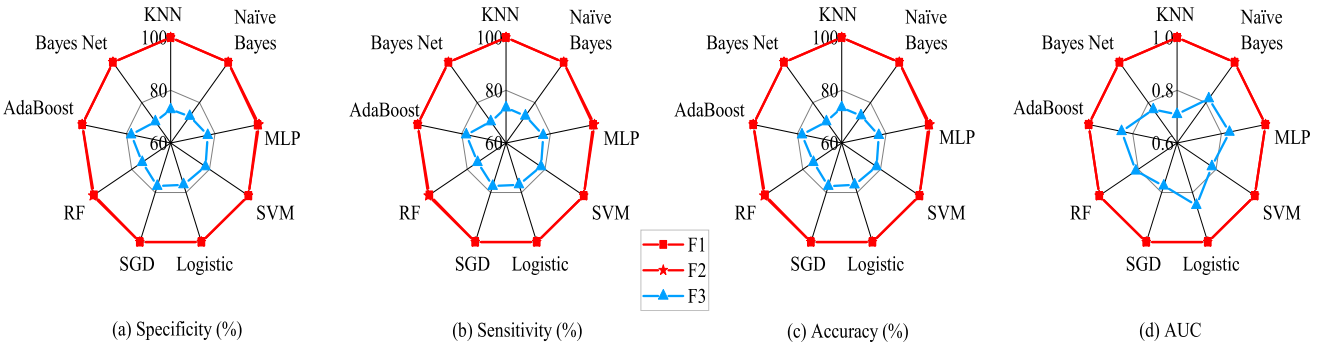

Fig. 6. The classification performance (accuracy, specificity, sensitivity, and AUC) for the features we developed to distinguish ADHD patients from HCs using the NYU training set. Note: The results obtained using features extracted from BOLD signals at the frequency bands F1 and F2 are presented in red because they are the same. It should also be noted that the performance was assessed based on 10-fold CV.

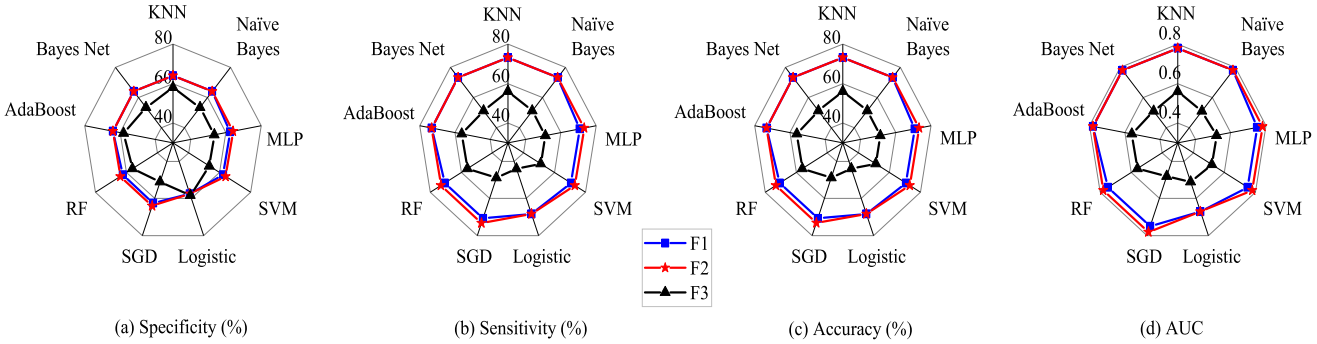

Fig. 7. The classification performance for the features we developed to identify ADHD patients from HCs using the NYU test set.

TABLE II
NUMBERS OF ROIS WITH SIGNIFICANT MAGNITUDES AND PHASES IN THE STABLE AND UNSTABLE DMS

Type of DM	Feature	F1	F2	F3
Stable	Magnitude	904	927	8
	Phase	862	828	0
Unstable	Magnitude	934	917	23
	Phase	929	899	104

Note: The total number of ROIs is 954; All results obtained after Bonferroni correction.

magnitudes and phases in both stable and unstable DMs at frequency bands F1 and F2 after Bonferroni correction were higher than those at frequency band F3 (observed using (23) – (26) in methods section). Additionally, we found that those ROIs with significant magnitudes and phases at all frequency bands were mainly from temporal lobe and cerebellum for all subjects from the five mentioned imaging sites.

Since it is almost impossible to illustrate the average magnitudes and phases of each ROI in stable and unstable DMs observed in (23) – (26), as described in the method section, we calculated the mean magnitudes and phases of all ROIs for each subject; the results are shown in Fig. 5. As can be seen, the magnitudes and phases of the ROIs in the stable and unstable DMs of the BOLD signals within all frequency bands were significant, except the phases of ROIs in stable DMs at frequency band F3.

B. Classification Performance

As mentioned in the methods section, ten features (as shown in Fig. 4 and Fig. 5) were used for ADHD detection. For the training set, as shown in Fig. 6: (1) At both frequency bands F1 and F2, all the classifiers accurately identified ADHD at highest possible precision, recall, and accuracy values of 100%. (2) At frequency band F3, all the classifiers accurately classified ADHD patients and HCs, especially SGD, AdaBoost, and SVM whose respective accuracy values were 77.4%, 77.9%, and 77.9%. For the testing set, at both frequency bands F1 and F2, the highest accuracy value of 73.2% was achieved using the KNN, Naïve Bayes, AdaBoost and Bayes Net classifiers (see Fig. 7).

Finally, we compared our proposed approach for ADHD detection with those of previous studies. As can be seen in Table III, for the training set, our proposed method outperformed all other existing methods. For the testing set, our method is still promising using the extracted features from BOLD signals within at least one frequency band of subjects from each site, which demonstrates the potential of our proposed method (see Table IV).

IV. DISCUSSION

In this study, we proposed a new perspective for analyzing fMRI BOLD signals: analyzing the stability of BOLD signals

TABLE III
PERFORMANCE COMPARISON OF THE PROPOSED METHOD WITH THE EXISTING APPROACHES FOR ADHD DIAGNOSIS USING TRAINING SET FROM ADHD-200

Author	Method	Dataset	Spec. (%)	Sens. (%)	Acc. (%)
Cheng *et al.* [32]	Brain network and topology attributes	Peking	85.1	63.3	76.1
Dey *et al.* [28]	Brain network and topology attributes	KKI	100	9.5	75.6
		NI	68.1	58.8	64.1
		Peking	96.6	21.1	61.2
		OHSU	65.8	53.5	60.6
Siquiera *et al.* [29]	Brain network and topology attributes, pattern recognition	NYU	58	68	63
		KKI	80	29	54
		NI	61	68	65
		Peking	65	50	57
		OHSU	83	63	73
Jie *et al.* [30]	Brain network and topology attributes	NYU	81.6	83.9	82.9
Riaz *et al.* [34]	Affinity propagation clustering	NYU	39.8	63.5	52.7
		KKI	90.1	77.2	86.7
		NI	73.9	72	72.9
		Peking	88.5	79.1	85.8
Shao *et al.* [33]	Brain network and topology attributes	NYU	N/R	N/R	72
		KKI	N/R	N/R	76
		Peking	N/R	N/R	82.6
Current study	**DMD Frequency band:**				
	-F1 (0.009-0.027 Hz)	NYU	100	100	100
		KKI	88.4	88.5	88.5
		NI	89.6	90	90
		Peking	97.6	97	96.9
		OHSU	91.7	91.1	91.1
	-F2 (0.027-0.073 Hz)	NYU	100	100	100
		KKI	91.3	91	91
		NI	94.9	94.9	94.9
		Peking	97.6	97.5	97.5
		OHSU	87.3	87.3	87.3
	- F3 (0.009-0.08 Hz)	NYU	77.9	78	77.9
		KKI	96	96.2	96.2
		NI	94.8	94.9	94.9
		Peking	96.5	95.1	95.1
		OHSU	92.8	92.4	92.4

Note: Spec.: specificity; Sens.: sensitivity (or recall); Acc.: Accuracy; N/R: not reported; fALFF: Fractional amplitude of low-frequency fluctuation; F1, F2 and F3: BOLD signal sub-frequency bands. References [28], [29], [30], and [32] all used brain network and topology attributes, but their network construction approaches and corresponding topology attributes differ. For more details, refer to the references. It should also be noted that all of these existing methods were further evaluated based on cross-validation.

TABLE IV
PERFORMANCE COMPARISON OF THE PROPOSED METHOD WITH THE EXISTING APPROACHES FOR ADHD DIAGNOSIS USING TEST SET FROM ADHD-200

Author	Method	Dataset	Spec. (%)	Sens. (%)	Acc. (%)
Colby *et al.* [31]	Brain network and topology attributes	NYU	58	34	37
		KKI	100	0	73
		NI	86	45	68
		Peking	96	25	57
Kuang *et al.* [35]	Deep belief network	NYU	N/R	N/R	37
		KKI	N/R	N/R	73
		Peking	N/R	N/R	54
Dey *et al.* [28]	Brain network and topology attributes	KKI	62.5	33.3	54.5
		NI	64.3	27.3	48
		Peking	92.6	20.8	58.8
		OHSU	78.6	53.6	68.2
Hao *et al.* [27]	Deep belief network and deep Bayesian network	NYU	68.8	43.9	64.7
		KKI	83	55.6	59
		Peking	87.7	22.9	66.3
Riaz *et al.* [34]	Affinity propagation clustering	NYU	41.6	68.9	60.9
		KKI	75	100	81.8
		NI	42.8	45.9	44.0
		Peking	92.6	33.3	64.7
Miao *et al.* [22]	fALFF, PCA, Shannon, and Sample Entropy	NYU	8.3	96.5	70.7
		KKI	87.5	66.7	81.8
		NI	92.9	54.5	76
		Peking	74.1	62.5	68.6
Current study	**DMD Frequency band:**				
	-F1 (0.009-0.027 Hz)	NYU	71.4	73.2	73.2
		KKI	81.8	81.8	81.8
		NI	78.6	76	76
		Peking	72	74.5	74.5
		OHSU	68.8	64.7	64.7
	-F2 (0.027-0.073 Hz)	NYU	71.4	73.2	73.2
		KKI	100	100	100
		NI	64.8	68	68
		Peking	67.2	68.6	68.6
		OHSU	66.7	71.4	70.5
	- F3 (0.009-0.08 Hz)	NYU	63.5	68.3	68.3
		KKI	91	90.9	90.9
		NI	87.6	88	88
		Peking	67.2	68.6	68.6
		OHSU	72.6	73.5	73.5

based on their stable and unstable modes decomposed using DMD. It is worth mentioning that in contrast with other existing methods to decompose BOLD signals, such as ICA and PCA, only DMD can extract components with their corresponding stabilities. Their eigenvalues can determine whether the corresponding dominant eigenvectors (or modes) are stable or unstable (see Fig. 2). Furthermore, DMD is able to reflect spatial patterns with dynamic temporal patterns of the fMRI data, whereas ICA and PCA cannot capture its temporal behaviors reflecting brain activity.

As mentioned in the introduction, this study hypothesized that brain disorders influence the stability of the DMs in BOLD signals, and the results conform to our hypothesis. For each BOLD common frequency band (F1, F2 and F3), as mentioned in the methods section, we extracted features to reflect the relationship between stable and unstable DMs. Then, Wilcoxon rank-sum test was conducted on each feature to assess whether the DM stability of BOLD signals from ADHD patients and HCs groups differed significantly ($p < 0.05$ after Bonferroni correction). Interestingly, most of the derived parameters were significant, especially in the frequency bands F1 and F2. This is consistent with previous studies, which have suggested that the subcomponents of BOLD signals at these frequency bands may reflect different underlying brain patterns and cognitive processes [40]. Also, this indicates that our proposed approach can generally be effective in distinguishing between these groups. Furthermore, as shown in Fig. 4, ADHD patients show more instability in DMs of BOLD signals at the frequency bands F1 and F2 compared with HCs. This may be due to the presence of structural and functional brain abnormalities

among ADHD patients, such as in the frontal cortex, cerebellum, and subcortical structures [51]. All of these observed results conform to the findings of previous studies, which have suggested that stability changes in individuals' physiological signals illuminates their pathological conditions. Additionally, according to system science theory, stable subsystems generally contribute to the efficiency, order, and adaptability of the whole system, whereas unstable subsystems do the opposite. In our study, we also found the same phenomenon in the brain system, i.e. the DMs of BOLD signals are more stable in HCs than in ADHD patients, which demonstrates that their brain systems of HCs function efficiently, orderly, and adaptively compared to those of ADHD patients.

However, we also found some interesting phenomena: (1) For all subjects from the four mentioned sites, we found that the ROIs with significant magnitudes and phases mainly came from the temporal lobe (including inferior, middle, and superior temporal gyrus, hippocampus, and parahippocampus) and cerebellum (including cerebellum crus and vermis). These ROIs are consistent with the existing clinical findings of ADHD. It has been reported that ADHD patients exhibit abnormal activation patterns in the temporal lobe, which is related to verbal memory and language [52]. Similarly, several studies have reported that the cerebellum, which plays an important role in motor control and cognitive functions, malfunctions in the case of ADHD [53]. (2) Furthermore, we found inconsistent trends in phases and magnitudes of ROIs between stable and unstable DMs (see Fig. 5). This can indicate that these parameters can reveal different physiological information, thus it is essential to consider both of them for analysis.

In order to further evaluate the effectiveness of our proposed approach, nine different classifiers were used, since they utilize different techniques for data classification. Encouragingly, as illustrated in Fig. 6, each of the classifiers was able to accurately distinguish HCs from ADHD patients at all frequency bands, especially at F1 and F2. This may be due to the following reasons: (1) In [42], children with ADHD exhibited BOLD time series fluctuations with significant higher power within frequency band F2 than healthy children. (2) Also, most information of the BOLD signals related to resting-state functional connectivity were found to be lying within frequency bands F1 and F2 [43]. Thus, our findings support the evidence that BOLD signals within frequency bands F1 and F2 provide essential diagnostic information for ADHD [42]. In addition, as can be seen in Tables III and IV, our proposed approach outperforms the existing methods for ADHD detection in classifying subjects from all five imaging sites. As can be seen in Table IV, even though the specificity (or sensitivity) values achieved by some existing methods on data taken from some sites are high, their observed sensitivity (or specificity) values are relatively low. However, our proposed method achieved encouraging results (both specificity and sensitivity values). This demonstrates the potential of our proposed method for fMRI BOLD signal analysis, which can assist clinicians to enhance automated diagnosis of ADHD.

In order to further demonstrate the improvement of our proposed approach, we carried out a supplementary analysis. We evaluated whether the age and sex of the ADHD patients and HCs taken from the five sites differed significantly. We found that the age and sex of subjects taken from NYU were not matched (p value < 0.05), and the sex of subjects taken from NI, Peking and OHSU, was also not matched. In order to eliminate the age and gender factors which may affect our conclusion, we excluded some subjects to match the age and sex of ADHD patients and HCs taken from the mentioned sites. We found that the results were the same as those from the complete samples. Additionally, in classifying age- and sex-matched subjects from all five imaging sites: (1) Using features from BOLD signals at frequency band F1, we achieved respective average precision, recall, accuracy, and AUC values of 94.2%, 94.10%, 94.07%, and 0.938. (2) At frequency band F2, the respective average precision, recall, accuracy, and AUC values were 95.43%, 95.35%, 95.12%, and 0.96. (3) Using features from frequency band F3, we obtained respective average precision, recall, accuracy, and AUC values of 93.84%, 92.88%, 92.88%, and 0.94. These results are consistent with those from all subjects (see Table III), which demonstrates that the stability of BOLD signals is not affected by either age or sex. Also, in order to evaluate the effects of different window sizes and step sizes on our proposed approach, we also considered 16-frame, 24-frame, 40-frame and 48-frame windows sliding by 4 frames as well as 32-frame windows sliding by 8 frames, 12 frames, and 16 frames. The results are consistent with those from 32-frame windows sliding over 4 frames. This shows that our proposed method remains robust when using BOLD signals from different window and step sizes.

We further applied our proposed method on two other datasets: the Huaxi Hospital dataset (Chengdu city, Sichuan Province, P. R. China) and NEUROCON dataset of the Neurology Department of the University Emergency Hospital Bucharest, Romania. Huaxi Hospital provided rs-fMRI data from 22 ADHD patients (ages: 11.2 ± 1.3 years) and 16 age-matched HCs (ages: 10.8 ± 1.6 years). The NEUROCON dataset is available at http://fcon_1000.projects.nitrc.org/indi/retro/parkinsons.html, contains rs-fMRI data from 27 Parkinson's disease patients (ages: 68.7 ± 10.6 years) and 16 age-matched HCs (ages:67.6 ± 11.9 years). We assessed the performance of our proposed method on these two datasets and compared it with one of the common methods for fMRI analysis, known as brain network analysis. First, we constructed brain networks by Granger causality and phase locking value and extracted topological attributes (clustering coefficient, rich-club coefficient, network density, network strength, and average link strength) [54]–[56]. Then, the classification performance of the aforementioned classifiers was assessed based on 10-CV. As shown in Table V, for the Huaxi dataset, our proposed method achieved the maximum accuracy value of 94.7 % for detection of ADHD, outperforming those for brain network analysis (Granger causality and phase locking value). In addition, the accuracy value of 100% was achieved in identifying PD patients from HCs taken from the NEUROCON dataset, demonstrating the good generalization ability of our proposed method for diagnosis of brain-related pathologies.

TABLE V
PERFORMANCE COMPARISON OF THE PROPOSED METHOD WITH THE COMMON APPROACHES FOR ADHD AND PD DIAGNOSIS

Dataset	Freq. band	Method	Spec. (%)	Sens. (%)	Acc. (%)
Huaxi (for ADHD)	F1	BNC by GC	76.6	76.3	76.3
		BNC by PLV	87.5	86.8	86.8
		Ours	93.4	92.1	92.1
	F2	BNC by GC	81.9	81.6	81.6
		BNC by PLV	87.5	86.8	86.8
		Ours	94.7	94.7	94.7
	F3	BNC by GC	87.5	86.8	86.8
		BNC by PLV	84.3	84.2	84.2
		Ours	94.7	94.7	94.7
NEUROCON (for Parkinson's disease)	F1	BNC by GC	57.5	62.8	62.8
		BNC by PLV	57.5	62.8	62.8
		Ours	100	100	100
	F2	BNC by GC	86.0	86.0	86.0
		BNC by PLV	90.8	90.7	90.7
		Ours	100	100	100
	F3	BNC by GC	93.0	93.0	93.0
		BNC by PLV	90.8	90.7	90.7
		Ours	100	100	100

Note: Freq.: frequency; GC: granger causality; PLV: phase locking value.

Finally, several points related to this study need to be mentioned: (1) Although DMD has been recently implemented for fMRI analysis, it has only been used to evaluate its spatiotemporal characteristics, not the stability of DMs of BOLD signals. Therefore, this study has assessed how the stability of DMs (or subsystems) of BOLD signals affect their macrodynamic patterns, which can indicate underlying patterns of brain subsystems. In addition, we evaluated the stability of DMs within three common frequency bands of BOLD signals, however, more frequency bands should be considered in the future. (2) In this study, we employed ADHD for demonstrating our proposed approach, because there is large ADHD database, namely ADHD-200 database, that has already been preprocessed and has been used by many studies, which allowed us to easily compare our proposed approach with various existing methods. However, in the future, our proposed approach should be applied to other brain diseases, such as Alzheimer's, to evaluate its possibility for disease diagnosis. (3) Similar to rs-fMRI data, the data recordings of task-state fMRI are also multidimensional. Therefore, our proposed method might also be applied for task-state fMRI data analysis, which may unveil new brain mechanisms that cannot be obtained by traditional approaches.

V. CONCLUSION

According to previous studies, the stability of physiological signals generally reflects an individual's health condition. The experimental results of this study conform to our hypothesis that the stability of fMRI BOLD signals can play an important role in disease diagnosis, which has not previously been demonstrated. We also showed the significance of the system science perspective for analyzing fMRI BOLD signals, i.e. to regard BOLD signals as large-scale system and evaluating how the stability of their DMs (subsystems) affects its overall properties. Finally, the proposed approach has demonstrated the capability to provide significant physiological information which are not given by existing methods. We have also demonstrated its great potential and accuracy in illuminating individuals' health conditions. Thus, it might be widely employed in clinical studies, as well as in various fields related to engineering.

REFERENCES

[1] N. K. Logothetis, J. Pauls, M. Augath, T. Trinath, and A. Oeltermann, "Neurophysiological investigation of the basis of the fMRI signal," *Nature*, vol. 412, no. 6843, pp. 150–157, Jul. 2001.

[2] B. Biswal, F. Z. Yetkin, V. M. Haughton, and J. S. Hyde, "Functional connectivity in the motor cortex of resting human brain using echo-planar MRI," *Magn. Reson. Med.*, vol. 34, no. 4, pp. 537–541, Oct. 1995.

[3] D. Zhang *et al.*, "Preoperative sensorimotor mapping in brain tumor patients using spontaneous fluctuations in neuronal activity imaged with functional magnetic resonance imaging: Initial experience," *Neurosurgery*, vol. 65, no. 6, pp. 226–236, Dec. 2009.

[4] G. Chen *et al.*, "Classification of Alzheimer disease, mild cognitive impairment, and normal cognitive status with large-scale network analysis based on resting-state functional MR imaging," *Radiology*, vol. 259, no. 1, pp. 213–221, Apr. 2011.

[5] C.-Z. Zhu *et al.*, "Fisher discriminative analysis of resting-state brain function for attention-deficit/hyperactivity disorder," *NeuroImage*, vol. 40, no. 1, pp. 110–120, Mar. 2008.

[6] R. C. Dorf and R. C. Bishop, "Modern control systems," *IEEE Trans. Syst., Man, Cybern., Syst.*, vol. 11, no. 8, p. 580, Aug. 1981.

[7] F. Tahami, R. Kazemi, and S. Farhanghi, "A novel driver assist stability system for all-wheel-drive electric vehicles," *IEEE Trans. Veh. Technol.*, vol. 52, no. 3, pp. 683–692, May 2003.

[8] M. V. Cook, *Flight Dynamics Principles: A Linear Systems Approach to Aircraft Stability and Control*. London, U.K.: Butterworth, 2012.

[9] P. Kundur *et al.*, *Power System Stability and Control*. New York, NY, USA: McGraw-Hill, 1994.

[10] C. Bachmann, T. Tetzlaff, R. Duarte, and A. Morrison, "Firing rate homeostasis counteracts changes in stability of recurrent neural networks caused by synapse loss in Alzheimer's disease," *PLOS Comput. Biol.*, vol. 16, no. 8, Aug. 2020, Art. no. e1007790.

[11] G. Hocepied, A. Kacha, F. Grenez, and A. Nonclercq, "Stability analysis of epileptic EEG signals," in *Proc. 8th IEEE Int. Conf. BIBE*, Oct. 2008, pp. 1–5.

[12] L. A. Aguirre and Á. V. P. Souza, "Stability analysis of sleep apnea time series using identified models: A case study," *Comput. Biol. Med.*, vol. 34, no. 3, pp. 241–257, Apr. 2004.

[13] L. Glass and M. C. Mackey, "Pathological conditions resulting from instabilities in physiological control systems," *Ann. New York Acad. Sci.*, vol. 316, no. 1, pp. 214–235, Feb. 1979.

[14] K. K. Chen, J. H. Tu, and C. W. Rowley, "Variants of dynamic mode decomposition: Boundary condition, Koopman, and Fourier analyses," *J. Nonlinear Sci.*, vol. 22, no. 6, pp. 887–915, Apr. 2012.

[15] C. W. Rowley, I. Mezić, S. Bagheri, P. Schlatter, and D. S. Henningson, "Spectral analysis of nonlinear flows," *J. Fluid Mech.*, vol. 641, pp. 115–127, Dec. 2009.

[16] J. L. Proctor and P. A. Eckhoff, "Discovering dynamic patterns from infectious disease data using dynamic mode decomposition," *Int. Health*, vol. 7, no. 2, pp. 139–145, Mar. 2015.

[17] B. W. Brunton, L. A. Johnson, J. G. Ojemann, and J. N. Kutz, "Extracting spatial-temporal coherent patterns in large-scale neural recordings using dynamic mode decomposition," *J. Neurosci. Methods*, vol. 258, pp. 1–15, Jan. 2016.

[18] M. S. J. Solaija, S. Saleem, K. Khurshid, S. A. Hassan, and A. M. Kamboh, "Dynamic mode decomposition based epileptic seizure detection from scalp EEG," *IEEE Access*, vol. 6, pp. 38683–38692, 2018.

[19] J. Casorso, X. Kong, W. Chi, D. Van De Ville, B. T. T. Yeo, and R. Liégeois, "Dynamic mode decomposition of resting-state and task fMRI," *NeuroImage*, vol. 194, pp. 42–54, Jul. 2019.

[20] J. M. Kunert-Graf, K. M. Eschenburg, D. J. Galas, J. N. Kutz, S. D. Rane, and B. W. Brunton, "Extracting reproducible time-resolved resting state networks using dynamic mode decomposition," *Frontiers Comput. Neurosci.*, vol. 13, p. 75, Oct. 2019.

[21] C. Rosazza *et al.*, "Functional connectivity during resting-state functional MR imaging: Study of the correspondence between independent component analysis and region-of-interest-based methods," *Amer. J. Neuroradiol.*, vol. 33, no. 1, pp. 180–187, Jan. 2012.

[22] B. Miao, L. L. Zhang, J. L. Guan, Q. F. Meng, and Y. L. Zhang, "Classification of ADHD individuals and neurotypicals using reliable RELIEF: A resting-state study," *IEEE Access*, vol. 7, pp. 62163–62171, 2019.

[23] J. Lunze, "Stability analysis of large-scale systems composed of strongly coupled similar subsystems," *Automatica*, vol. 25, no. 4, pp. 561–570, Jul. 1989.

[24] M. J. Dorahy, *Diagnostic and Statistical Manual of Mental Disorders*, 5th ed. Washington, DC, USA: American Psychiatric Association, 2013.

[25] M. Nuñez-Garcia *et al.*, "FADR: Functional-anatomical discriminative regions for rest fMRI characterization," in *Proc. MLMI*, 2015, pp. 61–68.

[26] A. Tabas, E. Balaguer-Ballester, and L. Igual, "Spatial discriminant ICA for RS-fMRI characterisation," in *Proc. Int. Workshop Pattern Recognit. Neuroimag.*, Jun. 2014, pp. 1–4.

[27] A. J. Hao, B. L. He, and C. H. Yin, "Discrimination of ADHD children based on deep Bayesian network," in *Proc. ICBISP* 2015, pp. 1–6.

[28] S. Dey, A. R. Rao, and M. Shah, "Attributed graph distance measure for automatic detection of attention deficit hyperactive disordered subjects," *Frontiers Neural Circuits*, vol. 8, p. 64, Jun. 2014.

[29] A. D. S. Siqueira *et al.*, "Abnormal functional resting-state networks in ADHD: Graph theory and pattern recognition analysis of fMRI data," *Biomed. Res. Int.*, vol. 2014, Aug. 2014, Art. no. 380531.

[30] B. Jie, C.-Y. Wee, D. Shen, and D. Zhang, "Hyper-connectivity of functional networks for brain disease diagnosis," *Med. Image Anal.*, vol. 32, pp. 84–100, Aug. 2016.

[31] J. B. Colby, J. D. Rudie, J. A. Brown, P. K. Douglas, M. S. Cohen, and Z. Shehzad, "Insights into multimodal imaging classification of ADHD," *Frontiers Syst. Neurosci.*, vol. 6, p. 59, Aug. 2012.

[32] W. Cheng, X. Ji, J. Zhang, and J. Feng, "Individual classification of ADHD patients by integrating multiscale neuroimaging markers and advanced pattern recognition techniques," *Frontiers Syst. Neurosci.*, vol. 6, p. 58, Aug. 2012.

[33] L. Shao, Y. You, H. Du, and D. Fu, "Classification of ADHD with fMRI data and multi-objective optimization," *Comput. Methods Programs Biomed.*, vol. 196, Nov. 2020, Art. no. 105676.

[34] A. Riaz, M. Asad, E. Alonso, and G. Slabaugh, "Fusion of fMRI and non-imaging data for ADHD classification," *Comput. Med. Imag. Graph.*, vol. 65, pp. 115–128, Apr. 2018.

[35] D. Kuang, X. Guo, X. An, Y. Zhao, and L. He, "Discrimination of ADHD based on fMRI data with deep belief network," in *Proc. Int. Conf. Intell. Comput.*, in Lecture Notes in Computer Science: Including Lecture Notes in Artificial Intelligence, and Lecture Notes in Bioinformatics, 2014, pp. 225–232.

[36] P. Bellec, C. Chu, F. Chouinard-Decorte, Y. Benhajali, D. S. Margulies, and R. C. Craddock, "The neuro bureau ADHD-200 preprocessed repository," *NeuroImage*, vol. 144, pp. 275–286, Jan. 2017.

[37] J. H. Tu *et al.*, "On dynamic mode decomposition: Theory and applications," *ACM J. Comput. Dyn.*, vol. 1, no. 2, pp. 391–421, Jun. 2014.

[38] J. N. Kutz, *Dynamic Mode Decomposition: Data-Driven Modeling of Complex Systems*. Philadelphia, PA, USA: SIAM, 2016.

[39] M. H. Hayes, *Schaum's Outline of Digital Signal Processing*. New York, NY, USA: McGraw-Hill, 1998.

[40] X. N. Zuo *et al.*, "The oscillating brain: Complex and reliable," *NeuroImage*, vol. 49, no. 2, pp. 1432–1445, Jan. 2010.

[41] Z. Zhan *et al.*, "The contribution of different frequency bands of fMRI data to the correlation with EEG alpha rhythm," *Brain Res.*, vol. 1543, pp. 235–243, Jan. 2014.

[42] A. Di Martino *et al.*, "Decomposing intra-subject variability in children with attention-deficit/hyperactivity disorder," *Biol. Psychiatry*, vol. 64, no. 7, pp. 607–614, Oct. 2008.

[43] R. Salvador *et al.*, "A simple view of the brain through a frequency-specific functional connectivity measure," *NeuroImage*, vol. 39, no. 1, pp. 279–289, Jan. 2008.

[44] T. Cover and P. Hart, "Nearest neighbor pattern classification," *IEEE Trans. Inf. Theory*, vol. IT-13, no. 1, pp. 21–27, Jan. 1967.

[45] S. K. Pal and S. Mitra, "Multilayer perceptron, fuzzy sets, and classification," *IEEE Trans. Neural Netw.*, vol. 3, no. 5, pp. 683–697, Sep. 1992.

[46] J. A. K. Suykens and J. Vandewalle, "Least squares support vector machine classifiers," *Neural Process. Lett.*, vol. 9, no. 3, pp. 293–300, Jan. 1999.

[47] A. Liaw and M. Wiener, "Classification and regression by randomforest," *R News*, vol. 2, no. 3, pp. 18–22, Dec. 2002.

[48] W. Hu, W. Hu, and S. Maybank, "AdaBoost-based algorithm for network intrusion detection," *IEEE Trans. Syst., Man, Cybern. B, Cybern.*, vol. 38, no. 2, pp. 577–583, Apr. 2008.

[49] N. Friedman, D. Geiger, and M. Goldszmidt, "Bayesian network classifiers," *Mach. Learn.*, vol. 29, nos. 2–3, pp. 131–163, Nov. 1997.

[50] E. Frank *et al.*, "Weka—A machine learning workbench for data mining," in *Data Mining and Knowledge Discovery Handbook*. Boston, MA, USA: Springer, 2009, pp. 1269–1277.

[51] J. Biederman, "Attention-deficit/hyperactivity disorder: A selective overview," *Biol. Psychiatry*, vol. 57, no. 11, pp. 1215–1220, Jun. 2005.

[52] M. V. Cherkasova and L. Hechtman, "Neuroimaging in attention-deficit hyperactivity disorder: Beyond the frontostriatal circuitry," *Can. J. Psychiatry*, vol. 54, no. 10, pp. 651–664, Oct. 2009.

[53] M. E. Toplak, C. Dockstader, and R. Tannock, "Temporal information processing in ADHD: Findings to date and new methods," *J. Neurosci. Methods*, vol. 151, no. 1, pp. 15–29, Feb. 2006.

[54] M. Kamiński, M. Ding, W. A. Truccolo, and S. L. Bressler, "Evaluating causal relations in neural systems: Granger causality, directed transfer function and statistical assessment of significance," *Biol. Cybern.*, vol. 85, no. 2, pp. 145–157, Aug. 2001.

[55] J. P. Lachaux, E. Rodriguez, J. Martinerie, and F. J. Varela, "Measuring phase synchrony in brain signals," *Hum. Brain Mapping*, vol. 8, no. 4, pp. 194–208, Jan. 1999.

[56] M. Rubinov and O. Sporns, "Complex network measures of brain connectivity: Uses and interpretations," *NeuroImage*, vol. 52, no. 3, pp. 1059–1069, Sep. 2010.